

Teaching Video Diffusion Model with Latent Physical Phenomenon Knowledge

Qinglong Cao^{1,2} Ding Wang² Xirui Li² Yuntian Chen^{2*} Chao Ma¹ Xiaokang Yang¹

¹Shanghai Jiao Tong University ²Eastern Institute of Technology, Ningbo

Project webpage: <https://qinglongcao.xyz/TVML-Diffusion.github.io/>

*Corresponding author

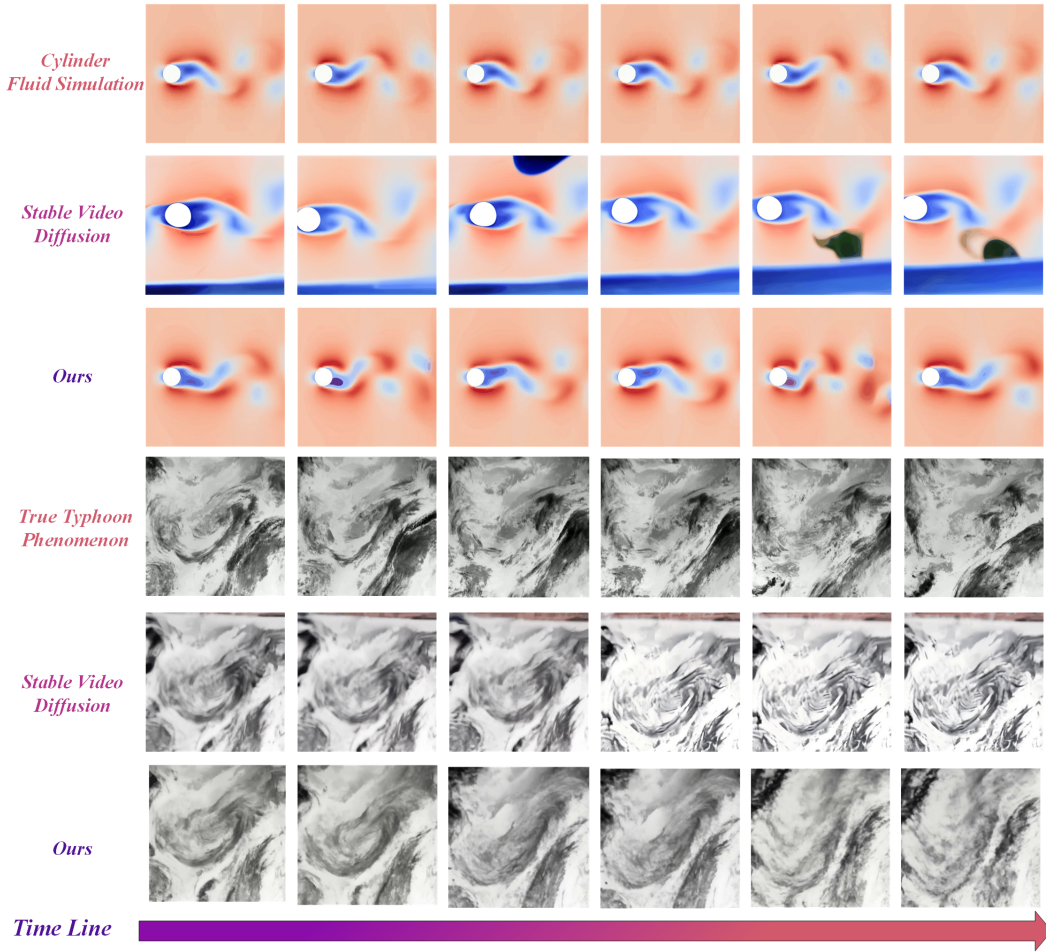


Figure 1. We propose a novel method to teach video diffusion models with latent physical phenomenon knowledge, enabling the accurate generation of physically informed phenomena.

Abstract

Video diffusion models have exhibited tremendous progress in various video generation tasks. However, existing models struggle to capture latent physical knowledge, failing to infer physical phenomena that are challenging to articulate with natural language. Generating videos following the fundamental physical laws is still an opening challenge. To address this challenge, we propose a novel method to teach video diffusion models with latent physical phe-

nomenon knowledge, enabling the accurate generation of physically informed phenomena. Specifically, we first pre-train Masked Autoencoders (MAE) to reconstruct the physical phenomena, resulting in output embeddings that encapsulate latent physical phenomenon knowledge. Leveraging these embeddings, we could generate the pseudo-language prompt features based on the aligned spatial relationships between CLIP vision and language encoders. Particularly, given that diffusion models typically use CLIP's language encoder for text prompt embeddings, our approach inte-

grates the CLIP visual features informed by latent physical knowledge into a quaternion hidden space. This enables the modeling of spatial relationships to produce physical knowledge-informed pseudo-language prompts. By incorporating these prompt features and fine-tuning the video diffusion model in a parameter-efficient manner, the physical knowledge-informed videos are successfully generated. We validate our method extensively through both numerical simulations and real-world observations of physical phenomena, demonstrating its remarkable performance across diverse scenarios.

1. Introduction

Diffusion models have made significant advances in understanding and generating media content [1, 4, 22, 36], allowing the creation of diverse, high-quality images [13, 49, 50]. However, because of the complexity of temporal motion and the high-dimension construction space, how to generate high-quality videos is still an open challenge. VDM [14] firstly attempts to apply diffusion models on video generation, providing promising results. Based on the training strategy [39], additional layers [3, 12], or fine-tuning [44], the T2I (Text-to-Image) models, many effective T2V (Text-to-Video) methods have been proposed based on the pre-trained T2I (Text-to-Image) models. More recently, based on the core idea of stable diffusion, stable video diffusion (SVD) [2] scales up the training data and achieves encouraging video generation performance.

However, whether video diffusion models can truly understand physical laws is still unexplored. To assess the capability of SVD in understanding physical laws, we apply it to both simulated and real-world physical phenomena: fluid simulation with strict physical law, and truly observed typhoon phenomenon with complex physical relations. As shown in Figure 1, SVD fails to capture the accurate evolution of physical changes, frequently producing unrealistic or hallucinated artifacts that deviate from expected physical behaviors. This failure indicates that SVD struggles to fully understand the latent physical knowledge. The camera-based vision videos used for training provide only basic spatiotemporal information, and the poor performance on our physical phenomena, governed by stronger and more complex physical constraints, further highlights this limitation. Collecting extensive physical simulation or observational data for directly training SVD remains challenging due to high resource costs. Moreover, naively fine-tuning with physical data alone does not enable video diffusion models to inherently learn physical laws, as shown in experiments. Consequently, how to generate videos that follow fundamental physical laws remains an opening challenge.

To tackle this challenge, we propose a novel approach to endow video diffusion models with latent physical phe-

nomenon knowledge, enabling the generation of physically informed videos. This capability is substantiated through evaluations across various phenomena with explicit physical metrics. The first main issue in incorporating physical knowledge is how to extract it. Inspired by the Masked Autoencoder (MAE) [9], which aims to recover the masked images, we believe through visually masking the physical phenomena, and leveraging the MAE to recover it, the output embedding of MAE could contain the latent physical phenomenon knowledge. The main reason is that to precisely recover the physical phenomena, the MAE has to understand the physical change and reconstruct the physical field with physical knowledge.

Another critical challenge in generating physically informed phenomena is effectively integrating latent physical phenomenon knowledge. Given the difficulty of describing physical phenomena in natural language and the central role of language prompts in diffusion models, we propose that physical knowledge-informed pseudo-language prompt features can serve as a viable solution. Particularly, since the powerful generalization ability of CLIP [32], existing diffusion models always tend to leverage the language encoder of CLIP to provide the text embeddings as the language prompt features. Moreover, the visual embeddings of CLIP, which could obtain for physical phenomena, are spatially aligned with the text embedding in a contrastive learning manner. Thus, the quaternion network [31], known for its effective spatial relation modeling ability, is leveraged to model the aligned spatial relationships. Under the guidance of latent physical phenomenon knowledge, the visual embeddings from the CLIP are propagated into the quaternion hidden space to analyze the spatial relationships and correspondingly produce the pseudo-language prompt features with physical knowledge.

Ultimately, by incorporating these prompt features and fine-tuning the stable video diffusion model in a parameter-efficient manner, we successfully generate physical phenomena that adhere to physical knowledge, as illustrated in Figure 1. In summary, our key contributions are as follows:

- To our knowledge, we propose the first approach to introduce latent physical phenomenon knowledge into the video diffusion models. It successfully teaches the video diffusion models to infer physical knowledge-informed phenomena.
- To address the challenge of articulating physical phenomena in natural language, we proposed a quaternion network-based method to effectively provide physical knowledge-informed pseudo-language prompt features, inspired by the aligned CLIP spatial relationships.
- We validate our method extensively through both numerical simulations and real-world observations of physical phenomena, demonstrating its superior performance across diverse scenarios.

2. Related Work

Diffusion-based Image Generation. Diffusion models [11, 41], inspired by nonequilibrium thermodynamics, have demonstrated remarkable performance across various tasks, particularly in image generation [5, 6]. For instance, Ho *et al.* [10] applied diffusion models with classifier-free guidance for efficient image generation, while Karras *et al.* [20] explored the design space of diffusion models to improve performance through better model architecture. Focusing on sampling efficiency, Salimans *et al.* [38] proposed new parameterizations and introduced progressive distillation to enhance diffusion models. Diffusion models have also been successfully applied in other tasks such as image restoration [21], image super-resolution [27], and image inpainting [29]. With the rise of large-scale vision-language pretraining [32], text-driven diffusion models [30, 33] have achieved substantial improvements in image generation. Notably, Ramesh *et al.* [33] directly used CLIP text embeddings to condition diffusion models, while Saharia *et al.* [37] incorporated large language models for text embeddings. Recently, Stable Diffusion [34] introduced a method that transfers diffusion to a latent embedding space, resulting in enhanced stability and performance, thus setting a new standard for generative models.

Diffusion-based Video Generation. Unlike images, videos require modeling complex motion and spatiotemporal relationships. Recent research [19, 46] has addressed these challenges by fine-tuning the image diffusion models or directly training with higher computing resources. For example, VideoLDM [3] performs temporal fine-tuning on stable diffusion for video generation, and TAV [44] fine-tunes image diffusion models in a parameter-efficient way to enable text-to-video generation. Ho *et al.* [14] extended 2D image diffusion to 3D video generation at low resolution, while Stable Video Diffusion (SVD) [2] employs a 3D UNet for high-resolution video generation in the latent diffusion space. Building on SVD, other approaches [23, 28] have pursued zero-shot video generation. Text2Video-Zero [23] encodes motion dynamics and fuses them using cross-frame attention for zero-shot generation, and VidToMe [28] enhances temporal consistency by integrating self-attention tokens across frames. Inspired by ControlNet [47], ControlVideo [48] enables controllable, training-free text-to-video generation.

3. Preliminaries

Latent Diffusion Model. Diffusion models [11, 40, 42] are a class of generative models based on an iterative denoising process. An image DM supposes a forward process where a clean image x_0 is corrupted by Gaussian noise ϵ ,

$$x_t = \sqrt{\alpha_t}x_0 + \sqrt{1 - \alpha_t}\epsilon, \quad (1)$$

where $t = 1, \dots, T$ is the current timestep and $\{\alpha_t\}$ are the monotonically decreasing noise schedule. Then, starting from random Gaussian noise, DM reverses the forward process to generate an image by estimating the noise direction and progressively denoising it.

Recent large-scale diffusion models [33, 34, 37] operate in the latent space to improve performance and efficiency. These latent diffusion models train an autoencoder [24] to map the image between pixel and latent space. Let $\mathcal{E}(\cdot)$ and $\mathcal{D}(\cdot)$ be the encoder and the decoder, where $\mathcal{E}(x) = z, \mathcal{D}(z) \approx x$. Both the training and inference are conducted in the latent space. Typically, a UNet [35] ϵ_θ is trained to estimate the noise with the objective

$$\min_{\theta} E_{z, \epsilon \sim \mathcal{N}(0, I), t} \|\epsilon - \epsilon_\theta(z_t, t, c)\|, \quad (2)$$

where c is the text embedding in text-to-image DMs. In this work, we base our experiments on stable video diffusion [2], a large-scale video latent diffusion model.

Quaternion Network. In four-dimensional space, a quaternion Q extends a complex number and can be expressed as follows:

$$Q = r\mathbf{1} + x\mathbf{i} + y\mathbf{j} + z\mathbf{k}, \quad (3)$$

where r , x , y , and z are real numbers, and $\mathbf{1}$, \mathbf{i} , \mathbf{j} , and \mathbf{k} are the quaternion unit basis. The real part of Q is denoted by r , while $x\mathbf{i} + y\mathbf{j} + z\mathbf{k}$ is the imaginary or vector part. Quaternions are useful for describing spatial relations because they contain embedded information that can be represented by a matrix of real numbers:

$$Q = \begin{bmatrix} r & -x & -y & -z \\ x & r & -z & y \\ y & z & r & -x \\ z & -y & x & r \end{bmatrix}. \quad (4)$$

The Hamilton product \otimes of two quaternions Q_1 and Q_2 is computed as:

$$\begin{aligned} Q_1 \otimes Q_2 = & (r_1 r_2 - x_1 x_2 - y_1 y_2 - z_1 z_2) \mathbf{1} \\ & + (r_1 x_2 + x_1 r_2 + y_1 z_2 - z_1 y_2) \mathbf{i} \\ & + (r_1 y_2 - x_1 z_2 + y_1 r_2 + z_1 x_2) \mathbf{j} \\ & + (r_1 z_2 + x_1 y_2 - y_1 x_2 + z_1 r_2) \mathbf{k}, \end{aligned} \quad (5)$$

A quaternion neural network can be defined as:

$$Q_{out} = \alpha(W \otimes Q), \quad (6)$$

where W represents the learnable parameters of the quaternion neural networks, \otimes denotes the Hadamard product, and α is the activation function defined as:

$$\alpha(Q) = f(r)\mathbf{1} + f(x)\mathbf{i} + f(y)\mathbf{j} + f(z)\mathbf{k}, \quad (7)$$

where f is any standard activation function.

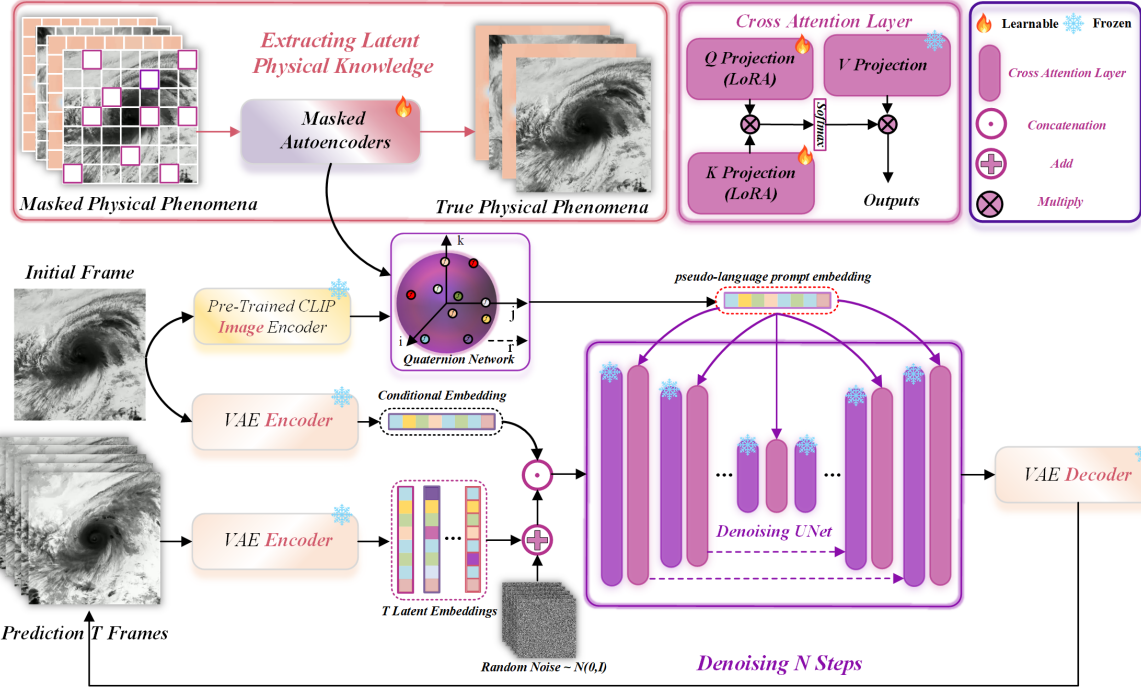


Figure 2. Overview of our proposed method. Aiming to teach stable video diffusion model with latent physical phenomenon knowledge. Using MAE to reconstruct masked physical phenomena. Projecting CLIP vision features into quaternion hidden space for pseudo-language embeddings enriched with latent physical phenomenon knowledge. Incorporating these embeddings and using parameter-efficient fine-tuning to make the model generate physically consistent phenomena.

4. Method

4.1. Video Generation Pipeline

Our goal is to equip the video diffusion model with latent physical phenomenon knowledge, enabling it to generate physically plausible phenomena from an initial frame, as shown in Figure 2. Given the initial frame f_0 of the target physical phenomenon \mathcal{V}_t with T frames $[f_1, f_2, \dots, f_T]$, we first propagate the initial frame through the VAE encoder and the CLIP image encoder to obtain conditional embeddings E_c and vision features F_o in the CLIP latent space, respectively. These embeddings serve as the initial conditional inputs. During the training phase, each frame of the target physical phenomenon \mathcal{V}_p is also passed through the VAE encoder to yield T latent embeddings that represent the phenomenon's evolving characteristics. Random noise is then added to these embeddings, resulting in the noisy inputs N_{input} , which simulate the diffusion process. For the inference phase, the random noise is sampled directly as noisy inputs, emulating initial randomness. The conditional embeddings E_c are concatenated with N_{input} to create the conditioned noisy inputs N'_{input} , establishing the connection between the initial frame and subsequent generation.

Following this, we employ the pre-trained Masked Autoencoders on the training physical phenomena to generate physical phenomenon knowledge-incorporated embeddings E_p from the initial frame. This embedding E_p captures the

latent physical attributes of the phenomenon and is crucial for generating coherent sequences. Both E_p and F_o are subsequently projected into quaternion space to model the spatially aligned vision-language relationships effectively, allowing us to derive the pseudo-language prompt embeddings E_L under the guidance of latent physical phenomenon knowledge. By integrating E_L into the cross-attention layer of the denoising UNet, and fine-tuning the network in a parameter-efficient manner using LoRA [15], the model iteratively denoises over T steps to generate the predicted physical frames \mathcal{V}_p . This integration ensures the generated frames remain consistent with the underlying physical laws across the sequence.

4.2. Latent Knowledge Extraction

Given K training physical phenomena $[\mathcal{V}_1, \mathcal{V}_2, \dots, \mathcal{V}_K]$ used during the learning process, each phenomenon is first divided into individual frames to construct a training image set. Each image is then partitioned into regular, non-overlapping patches to facilitate processing. A subset of these patches, denoted as P_{vis} , is randomly sampled and remains visible, while the remaining patches, labeled as P_{masked} , are masked out to encourage spatial prediction. Subsequently, we employ a Vision Transformer (ViT) [7] to form both the encoder and decoder components of the Masked Autoencoder (MAE). By only propagating the tokens of visible patches, the model aims to reconstruct the

pixel values of the masked patches as the supervision target. Formally, the masked patch predictions can be expressed as follows:

$$P_{\text{masked}} = \text{MAE}(P_{\text{vis}}). \quad (8)$$

The mean squared error (MSE) between the reconstructed and original images in pixel space serves as the loss function, driving the model towards accurate reconstruction. This process encourages the MAE to fully capture the physical characteristics of each phenomenon. As a result, the embeddings E_p from the MAE decoder contain rich latent representations of the physical knowledge embedded within the training phenomena, providing a comprehensive understanding crucial for downstream video generation tasks.

4.3. Quaternion Network Projection

Normally, video diffusion models heavily depend on language prompts as core inputs to drive meaningful video generation. However, physical phenomena are challenging to describe directly with natural language. Notably, many video diffusion models utilize the CLIP text encoder to generate text embeddings as prompt features. CLIP aligns images and their corresponding text embeddings by maximizing the cosine similarity for matched pairs and minimizing it for unmatched pairs, thereby establishing robust vision-language relationships that can extend across various applications. Leveraging these stable vision-language relationships, alongside the acquirable visual features, allows us to derive pseudo-language prompt features that serve as effective prompts for language descriptions in video generation.

Quaternion Network is known for its powerful spatial relationship modeling ability [31]. Thus, we adopt quaternion networks to model the aligned spatial relationships and produce the pseudo-language prompt features. Furthermore, since the CLIP is pre-trained in the natural images, which could not align with the physical phenomenon, the latent physical knowledge should be added to support this modeling. Particularly, by propagating the initial frame into the CLIP vision encoder and pre-trained MAE, we could obtain the vision features E_p and latent knowledge-incorporated embeddings F_o . To better model the aligned relationships in the quaternion latent space, two separately linear layers [L_{d1}, L_{d2}] are applied on F_o and E_p to obtain the projected vision features \widehat{F}_o and projected knowledge-incorporated embeddings \widehat{E}_p :

$$\widehat{F}_o = L_{d1}(F_0); \widehat{E}_p = L_{d2}(E_p), \quad (9)$$

Additionally, we initialize learnable text embeddings T_L to further support the alignment process. The embeddings \widehat{E}_p , \widehat{F}_o , and T_L are then positioned along three orthogonal axes in the quaternion latent space as follows:

$$Q_l = T_L + \widehat{E}_p \mathbf{i} + \widehat{F}_o \mathbf{j} + 0 \mathbf{k}, \quad (10)$$

To complete the quaternion projection, we introduce a zero tensor Z_0 matching the dimensions of T_L . Correspondingly, given quaternion layer Q_t , the generation of pseudo-language prompt embeddings enriched with physical knowledge E_L is computed as follows:

$$E_L = Q_t([T_L, \widehat{E}_p, \widehat{F}_o, Z_0]), \quad (11)$$

4.4. Teaching Latent Knowledge

With the critical pseudo-language prompt embeddings E_L providing latent physical phenomenon knowledge, we guide the stable video diffusion model by efficiently fine-tuning the cross-attention layer of the UNet. Formally, in the cross-attention layer, the flattened intermediate representation of the UNet, z_t , and the prompt features, y , are first projected to intermediate representations $\varphi_i(z_t) \in \mathbb{R}^{N \times d_\epsilon^i}$ and $\tau_\theta(y) \in \mathbb{R}^{M \times d_\tau}$, which are then mapped to the intermediate layers of the UNet via a cross-attention mechanism that implements $\text{Attention}(Q, K, V) = \text{softmax}\left(\frac{QK^T}{\sqrt{d}}\right) \cdot V$. To enable efficient learning, LoRA [15] is applied to the Q and K matrices, with the prompt features provided by E_L . Thus, the learning process functions as follows:

$$\begin{aligned} Q &= \text{LoRA}(W_Q^{(i)}) \cdot \varphi_i(z_t), \\ K &= \text{LoRA}(W_K^{(i)}) \cdot \tau_\theta(E_L), \\ V &= W_V^{(i)} \cdot \tau_\theta(E_L). \end{aligned} \quad (12)$$

Here, $W_V^{(i)} \in \mathbb{R}^{d \times d_\epsilon^i}$, $W_Q^{(i)} \in \mathbb{R}^{d \times d_\tau}$, and $W_K^{(i)} \in \mathbb{R}^{d \times d_\tau}$ are the projection matrices. Aside from the LoRA layers, all other parameters remain frozen, ensuring efficient parameter usage.

Overall, given the stable video diffusion model D_t , the CLIP image encoder E_{img} , and the quaternion projection process Q , the generation process is defined as follows:

$$\mathcal{V}_p = D_t([DDIM_{\text{sample}}, F_0], Q(E_{\text{img}}(f_0), \text{MAE}(f_0))). \quad (13)$$

5. Experiments

5.1. Experiment Setting

We adopt SVD [2] as the baseline video generation model and conducted experiments on both simulation fluid phenomenon datasets and true typhoon phenomenon datasets. Metrics across numerical precision and physical statistics are leveraged to extensively evaluate our proposed method. All the source code and datasets will be released.

Datasets and Evaluation Metrics. We utilize the computational fluid dynamics (CFD) tool to generate four fluid simulation phenomena: Rayleigh-Bénard convection (RBC) simulation, Cylinder fluid simulation, DamBreak

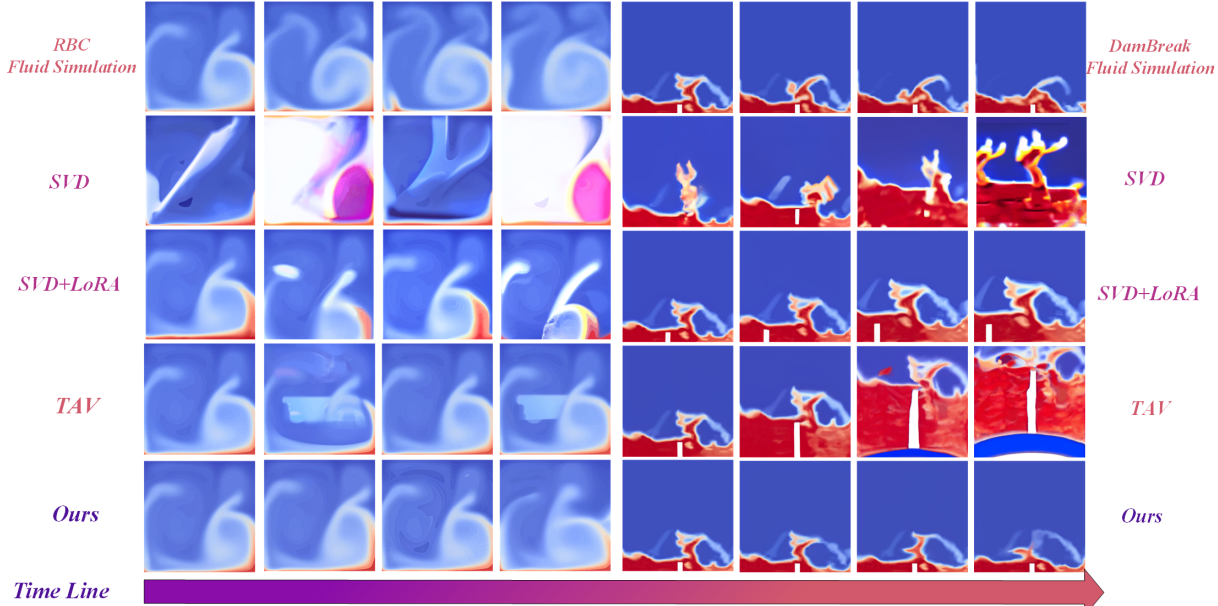


Figure 3. Qualitative comparison between our method and other advanced methods in fluid simulation dataset. Though incorporating physical phenomenon knowledge, our method generates rational phenomena that exhibit better alignment with physical laws.

fluid simulation, and DepthCharge fluid simulation, to validate our method within controlled numerical simulation scenarios. Additionally, to assess the model’s performance in real-world settings, we select four typhoon phenomena from the true typhoon dataset [25], with identifiers corresponding to observation dates: 202001, 202009, 202102, and 202204. Each fluid simulation or typhoon phenomenon consists of 10 videos; we randomly select 9 videos for fine-tuning and reserve the remaining video for testing.

To evaluate the generated physical phenomena, we consider eight essential metrics: RMSE, SSIM, Stream Function Error (SFE), Smoothness Error (SE), Gradient Smoothness (GS), Continuity Score (CS), Q-Criterion Error (QCE), and Vorticity Error (VE). RMSE and SSIM [43] are widely used metrics for assessing numerical accuracy and visual structural similarity. The other metrics are specialized physical measures tailored to evaluate the preservation of physical properties, which is the core objective of our approach. Specifically, SFE [8, 26] assesses streamline accuracy, while SE [18] measures stable propagation characteristics. GS and CS [26], two physical metrics without ground truth (GT), evaluate the reasonableness of the phenomenon’s progression and overall consistency, respectively. QCE [16] measures the preservation of vortex structures, and VE [17] assesses vorticity accuracy. QCE and VE required precise fields, which are only available for simulation data. Notably, while SSIM benefits from a higher score for better performance, lower scores indicate better outcomes for the other metrics. Further details on evaluation metrics are available in the supplementary material.

Implement Details. Apart from the pre-trained SVD, we use the pre-trained ViT-B/16 CLIP model for providing

visual features. The network is trained with a learning rate of $2e - 4$ using the SGD optimizer on the NVIDIA A100 GPUs. DDIM scheduler [41] with sampling step $T = 50$ is leveraged for sampling. The LoRA rank for fluid simulation phenomenon and true typhoon phenomenon are 4 and 8 respectively. The generated frame size is set as 512×512 .

5.2. Experimental Results

Qualitative Evaluation. To qualitatively assess the performance of our proposed method, we conducted a comparative analysis with other advanced generation methods, with visual results provided in Figure 3 and Figure 4. Specifically, for methods like TAV [44] and SimDA [45], we follow the previous methods to either use the initial frame as a prompt or concatenate it with input noise. In Figure 3, which presents outcomes on the fluid simulation dataset, we observe that existing video diffusion models often struggle to capture the underlying physical phenomena. For instance, SVD tends to produce visual artifacts and hallucinations that deviate from real-world interpretations, leading to outputs that cannot be accurately perceived, such as fluid appearing like upward-growing flowers or flames. Even with improvements through LoRA fine-tuning or advanced TAV methods, these models continue to produce results that contradict fundamental physical laws. For example, in the DamBreak fluid simulation, these models fail to depict fluid movement realistically, treating it more like static or upward motion. In contrast, our method, provided with an initial frame, generates videos that visually align with physical principles, although they may not precisely replicate GT frames.

Similarly, qualitative comparisons on the true typhoon

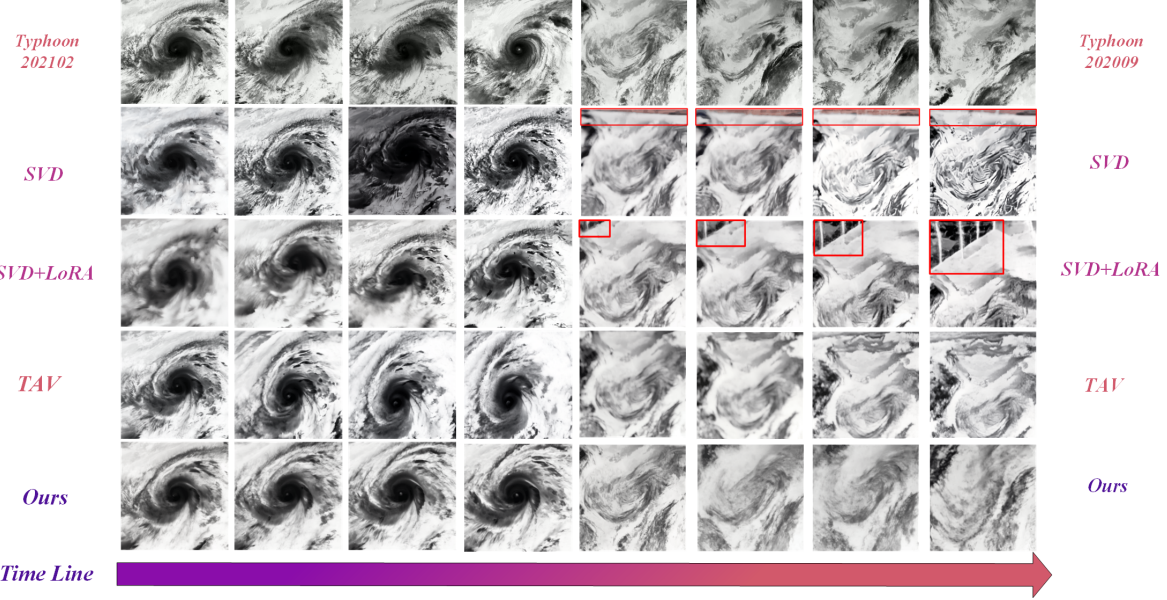


Figure 4. Qualitative comparisons in true typhoon dataset. Red box denotes some hallucinations. We highly recommend reviewers to view our video results in supplementary materials.

	RMSE↓	SSIM↑	SFE↓	SE↓	GS↓	CS↓	QCE↓	VE↓		RMSE↓	SSIM↑	SFE↓	SE↓	GS↓	CS↓
<i>RBC fluid simulation</i>								<i>Typhoon 20001</i>							
SVD	9.323	0.773	170.48	1.893	4.826	12.46	0.075	0.029		9.702	0.365	1575.8	2.942	20.26	16.66
LoRA*	8.876	0.831	82.159	0.609	3.670	5.773	0.018	0.004		9.642	0.395	2733.6	7.240	17.32	31.21
TAV	8.457	0.863	15.470	0.229	2.731	1.706	0.003	6e-4		9.696	0.367	3297.7	15.53	18.94	37.20
SimDA	8.786	0.857	14.895	0.256	3.012	1.716	0.003	8e-4		9.710	0.375	2846.3	14.67	18.37	34.61
Ours	8.585	0.885	5.6910	0.120	2.514	1.009	0.001	2e-4		9.525	0.427	937.56	1.529	11.35	23.29
<i>Cylinder fluid simulation</i>								<i>Typhoon 202009</i>							
SVD	8.081	0.871	399.88	1.453	4.832	15.83	0.211	0.022		10.29	0.308	3443.9	7.828	18.94	32.44
LoRA*	7.206	0.906	185.33	0.760	3.921	9.221	0.046	0.014		10.16	0.367	4113.3	2.793	12.02	29.51
TAV	7.710	0.891	178.10	0.633	4.420	6.693	0.027	0.007		10.17	0.360	2812.0	2.455	9.752	21.09
SimDA	7.682	0.883	180.45	0.667	4.012	6.721	0.031	0.006		10.15	0.357	2965.1	2.832	9.212	25.61
Ours	5.975	0.949	78.739	0.405	2.631	5.876	0.021	0.003		9.953	0.406	1319.3	2.652	8.494	21.98
<i>DamBreak fluid simulation</i>								<i>Typhoon 202102</i>							
SVD	8.189	0.743	1388.6	7.686	9.483	51.69	0.539	0.205		10.08	0.250	3290.9	8.953	17.99	20.35
LoRA*	5.812	0.786	392.37	1.233	6.471	15.97	0.257	0.021		9.981	0.319	6264.3	17.94	16.48	49.02
TAV	7.792	0.686	1543.6	2.572	10.08	34.33	0.205	0.140		10.07	0.298	3440.6	3.429	14.46	25.95
SimDA	7.679	0.691	1243.5	2.667	9.892	36.55	0.281	0.161		10.06	0.308	2898.5	3.509	14.01	26.07
Ours	5.165	0.861	159.95	0.516	3.475	11.57	0.052	0.010		9.847	0.348	1016.4	2.297	10.79	20.01
<i>DepthCharge fluid simulation</i>								<i>Typhoon 202204</i>							
SVD	9.745	0.690	899.84	6.716	11.04	48.52	0.488	0.236		9.760	0.358	2624.2	7.883	15.78	39.09
LoRA*	7.916	0.733	2213.9	7.405	13.19	75.91	1.300	0.482		9.677	0.338	1860.4	4.660	14.52	22.66
TAV	7.679	0.734	1307.7	5.777	13.04	61.66	0.587	0.256		9.649	0.359	2357.3	7.702	14.67	32.52
SimDA	7.682	0.745	1298.2	5.867	14.01	67.21	0.576	0.301		9.686	0.347	2657.1	7.919	15.12	31.89
Ours	4.711	0.819	311.10	2.683	8.601	24.84	0.126	0.062		9.529	0.405	1625.1	2.995	11.10	22.70

Table 1. Quantitative evaluation results on fluid simulation dataset (Left Side) and true typhoon dataset (Right Side). SVD: Stable Video Diffusion [2]. LoRA*: SVD+LoRA [15]. TAV: Tune-A-video [44]. SimDA: Simple Diffusion Adapter [45].

dataset, visualized in Figure 4, reveal similar challenges for baseline methods. SVD continues to generate implausible visual artifacts that do not adhere to physical laws, and even with LoRA fine-tuning or advanced TAV methods, the resulting videos lack accurate representations of the physical

processes. In some cases, input frames are misinterpreted, leading to unnatural views such as the scene being mistaken for a snowy mountain or leather from varying perspectives. In contrast, our method demonstrates a better grasp of physical realism, producing predictions that, while not identical

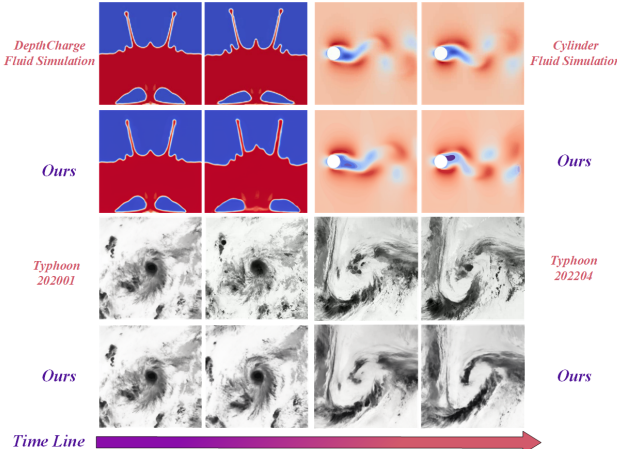


Figure 5. More qualitative results of our proposed method.

to GT, respect fundamental physical laws and more closely approximate the true phenomena. To further illustrate the effectiveness of our approach, Figure 5 provides additional visualization samples from various scenarios. These examples consistently highlight the superior performance of our method, demonstrating its robustness and alignment with physical realism across different cases.

Quantitative Evaluation. To objectively evaluate the effectiveness of our proposed method, we compared it with eight other methods across both numerical accuracy and physical measurement metrics, as shown in Table 1. Overall, our method demonstrates a clear advantage, achieving superior performance across the majority of metrics. Specifically, in the fluid simulation dataset, our method exhibits notable improvements in physical metrics, underscoring its ability to generate phenomena informed by physical principles. Notably, the most substantial performance gain is observed in SFE, suggesting that our method more accurately predicts physical streamlines and reconstructs dynamics with greater physical fidelity. Our method achieved top performance in most metrics, with one exception: the RMSE in the RBC fluid simulation, suggesting that additional training samples may be beneficial to further enhance numerical accuracy. In the more challenging true typhoon dataset, our method continues to show strong overall performance, consistently generating phenomena that adhere closely to physical laws. However, in the CS metric, which evaluates video consistency in the absence of GT, our method did not achieve the highest score. We believe this may be due to the inherent nature-vision consistency bias in pre-trained video diffusion models. Incorporating physical knowledge with limited samples may not fully alter this pattern to fit the target domain, presenting an area for further improvement in future work.

	RMSE↓	SSIM↑	SFE↓	SE↓	GS↓	CS↓	QCE↓	VE↓
w/o PK	7.523	0.873	181.46	0.713	4.021	8.146	0.035	0.008
w/o QM	6.876	0.921	112.16	0.579	3.134	5.987	0.026	0.005
Ours	5.975	0.949	78.739	0.405	2.631	5.876	0.021	0.003

Table 2. Ablation study on cylinder fluid simulation. w/o: without, PK: physical phenomenon knowledge, QM: quaternion spatial modeling. Best result is bolded.

Rank	RMSE↓	SSIM↑	SFE↓	SE↓	GS↓	CS↓	QCE↓	VE↓
2	6.013	0.939	80.124	0.453	2.721	5.976	0.031	0.004
4	5.975	0.949	78.739	0.405	2.631	5.876	0.021	0.003
8	6.171	0.932	82.159	0.479	2.834	6.017	0.029	0.005

Table 3. Ablation study of LoRA rank on cylinder fluid simulation.

5.3. Ablation Study

To assess the impact of incorporating physical phenomenon knowledge and quaternion spatial modeling, we conducted an ablation study by setting the knowledge-incorporated embeddings to zero and replacing quaternion networks with standard neural networks. These experiments were performed on the cylinder fluid simulation dataset, with results summarized in Table 2. The findings clearly indicate that the inclusion of physical phenomenon knowledge is crucial to enhancing model performance, while quaternion spatial modeling further refines the results, enabling more accurate alignment with physical dynamics. Additionally, we performed an ablation study on the LoRA rank to identify the optimal parameter setting. As shown in Table 3, we selected the rank that yielded the best performance for our experiments, confirming that tuning the rank is essential for achieving the most reliable results.

6. Conclusion

Current video diffusion models struggle to understand latent physical knowledge, limiting their capacity to generate phenomena that adhere to the fundamental physical law. To address this limitation, we first utilize MAE to extract latent physical knowledge. Leveraging the robust alignment in CLIP’s vision-language relationship, we then propagate the CLIP visual features, guided by the extracted physical knowledge, into a quaternion hidden space to model the complex relationships and produce pseudo-language prompt features. By incorporating these prompt features and fine-tuning the video diffusion model parameter-efficiently, we enable the generation of physically realistic phenomena with an initial frame as input. Extensive experiments on both numerical simulations and real-world observations validate the effectiveness and superiority of our method, illustrating its potential to push the boundaries of physically informed video generation.

References

- [1] Tomer Amit, Tal Shaharbany, Eliya Nachmani, and Lior Wolf. Segdiff: Image segmentation with diffusion proba-

- bilistic models. *arXiv:2112.00390*, 2021. 2
- [2] Andreas Blattmann, Tim Dockhorn, Sumith Kulal, Daniel Mendelevitch, Maciej Kilian, Dominik Lorenz, Yam Levi, Zion English, Vikram Voleti, Adam Letts, et al. Stable video diffusion: Scaling latent video diffusion models to large datasets. *arXiv:2311.15127*, 2023. 2, 3, 5, 7
- [3] Andreas Blattmann, Robin Rombach, Huan Ling, Tim Dockhorn, Seung Wook Kim, Sanja Fidler, and Karsten Kreis. Align your latents: High-resolution video synthesis with latent diffusion models. In *Proceedings of the IEEE/CVF Conference on Computer Vision and Pattern Recognition*, 2023. 2, 3
- [4] Shoufa Chen, Peize Sun, Yibing Song, and Ping Luo. Diffusiondet: Diffusion model for object detection. In *Proceedings of the IEEE/CVF International Conference on Computer Vision*, 2023. 2
- [5] Florinel-Alin Croitoru, Vlad Hondu, Radu Tudor Ionescu, and Mubarak Shah. Diffusion models in vision: A survey. *IEEE Transactions on Pattern Analysis and Machine Intelligence*, 2023. 3
- [6] Prafulla Dhariwal and Alexander Nichol. Diffusion models beat gans on image synthesis. *Advances in Neural Information Processing Systems*, 2021. 3
- [7] Alexey Dosovitskiy. An image is worth 16x16 words: Transformers for image recognition at scale. *arXiv:2010.11929*, 2020. 4
- [8] Gunnar Farnebäck. Two-frame motion estimation based on polynomial expansion. In *Scandinavian Conference on Image Analysis*, 2003. 6, 1
- [9] Kaiming He, Xinlei Chen, Saining Xie, Yanghao Li, Piotr Dollár, and Ross Girshick. Masked autoencoders are scalable vision learners. In *Proceedings of the IEEE/CVF Conference on Computer Vision and Pattern Recognition*, 2022. 2
- [10] Jonathan Ho and Tim Salimans. Classifier-free diffusion guidance. *arXiv:2207.12598*, 2022. 3
- [11] Jonathan Ho, Ajay Jain, and Pieter Abbeel. Denoising diffusion probabilistic models. *Advances in Neural Information Processing Systems*, 2020. 3
- [12] Jonathan Ho, William Chan, Chitwan Saharia, Jay Whang, Ruiqi Gao, Alexey Gritsenko, Diederik P Kingma, Ben Poole, Mohammad Norouzi, David J Fleet, et al. Imagen video: High definition video generation with diffusion models. *arXiv:2210.02303*, 2022. 2
- [13] Jonathan Ho, Chitwan Saharia, William Chan, David J Fleet, Mohammad Norouzi, and Tim Salimans. Cascaded diffusion models for high fidelity image generation. *Journal of Machine Learning Research*, 2022. 2
- [14] Jonathan Ho, Tim Salimans, Alexey Gritsenko, William Chan, Mohammad Norouzi, and David J Fleet. Video diffusion models. *Advances in Neural Information Processing Systems*, 2022. 2, 3
- [15] Edward J Hu, Yelong Shen, Phillip Wallis, Zeyuan Allen-Zhu, Yuanzhi Li, Shean Wang, Lu Wang, and Weizhu Chen. Lora: Low-rank adaptation of large language models. *arXiv:2106.09685*, 2021. 4, 5, 7
- [16] J. C. R. Hunt, A. A. Wray, and P. Moin. Eddies, streams, and convergence zones in turbulent flows. In *Studying Turbulence Using Numerical Simulation Databases*, 2, 1988. 6, 3
- [17] Jinhee Jeong and Fazle Hussain. On the identification of a vortex. *Journal of Fluid Mechanics*, 1995. 6, 3
- [18] Jisoo Jeong, Jamie Menjay Lin, Fatih Murat Porikli, and Nojun Kwak. Imposing consistency for optical flow estimation. *Proceedings of the IEEE/CVF Conference on Computer Vision and Pattern Recognition*, 2022. 6, 1
- [19] Yuming Jiang, Tianxing Wu, Shuai Yang, Chenyang Si, Dahua Lin, Yu Qiao, Chen Change Loy, and Ziwei Liu. Videobooth: Diffusion-based video generation with image prompts. In *Proceedings of the IEEE/CVF Conference on Computer Vision and Pattern Recognition*, 2024. 3
- [20] Tero Karras, Miika Aittala, Timo Aila, and Samuli Laine. Elucidating the design space of diffusion-based generative models. *Advances in Neural Information Processing Systems*, 2022. 3
- [21] Bahjat Kawar, Michael Elad, Stefano Ermon, and Jiaming Song. Denoising diffusion restoration models. *Advances in Neural Information Processing Systems*, 2022. 3
- [22] Amirhossein Kazerouni, Ehsan Khodapanah Aghdam, Moein Heidari, Reza Azad, Mohsen Fayyaz, Ilker Hacihaliloglu, and Dorit Merhof. Diffusion models for medical image analysis: A comprehensive survey. *arXiv:2211.07804*, 2022. 2
- [23] Levon Khachatryan, Andranik Movsisyan, Vahram Tadevosyan, Roberto Henschel, Zhangyang Wang, Shant Navasardyan, and Humphrey Shi. Text2video-zero: Text-to-image diffusion models are zero-shot video generators. In *Proceedings of the IEEE/CVF International Conference on Computer Vision*, 2023. 3
- [24] Diederik P Kingma. Auto-encoding variational bayes. *arXiv:1312.6114*, 2013. 3
- [25] Asanobu Kitamoto, Jared Hwang, Bastien Vuillod, Lucas Gautier, Yingtao Tian, and Tarin Clanuwat. Digital typhoon: Long-term satellite image dataset for the spatio-temporal modeling of tropical cyclones. In *NeurIPS 2023 Datasets and Benchmarks*, 2023. 6
- [26] Pijush K. Kundu, Ira M. Cohen, and David R. Dowling. *Fluid Mechanics*. Elsevier, 6 edition, 2015. 6, 1
- [27] Haoying Li, Yifan Yang, Meng Chang, Shiqi Chen, Huajun Feng, Zhihai Xu, Qi Li, and Yueteng Chen. Srdiff: Single image super-resolution with diffusion probabilistic models. *Neurocomputing*, 2022. 3
- [28] Xirui Li, Chao Ma, Xiaokang Yang, and Ming-Hsuan Yang. Vidtome: Video token merging for zero-shot video editing. In *Proceedings of the IEEE/CVF Conference on Computer Vision and Pattern Recognition*, 2024. 3
- [29] Andreas Lugmayr, Martin Danelljan, Andres Romero, Fisher Yu, Radu Timofte, and Luc Van Gool. Repaint: Inpainting using denoising diffusion probabilistic models. In *Proceedings of the IEEE/CVF Conference on Computer Vision and Pattern Recognition*, 2022. 3
- [30] Alex Nichol, Prafulla Dhariwal, Aditya Ramesh, Pranav Shyam, Pamela Mishkin, Bob McGrew, Ilya Sutskever, and Mark Chen. Glide: Towards photorealistic image generation and editing with text-guided diffusion models. *arXiv:2112.10741*, 2021. 3

- [31] Titouan Parcollet, Mirco Ravanelli, Mohamed Mørchid, Georges Linarès, Chiheb Trabelsi, Renato De Mori, and Yoshua Bengio. Quaternion recurrent neural networks. *arXiv:1806.04418*, 2018. [2](#), [5](#)
- [32] Alec Radford, Jong Wook Kim, Chris Hallacy, Aditya Ramesh, Gabriel Goh, Sandhini Agarwal, Girish Sastry, Amanda Askell, Pamela Mishkin, Jack Clark, et al. Learning transferable visual models from natural language supervision. In *International Conference on Machine Learning*, 2021. [2](#), [3](#)
- [33] Aditya Ramesh, Prafulla Dhariwal, Alex Nichol, Casey Chu, and Mark Chen. Hierarchical text-conditional image generation with clip latents. *arXiv:2204.06125*, 2022. [3](#)
- [34] Robin Rombach, Andreas Blattmann, Dominik Lorenz, Patrick Esser, and Björn Ommer. High-resolution image synthesis with latent diffusion models. In *Proceedings of the IEEE/CVF Conference on Computer Vision and Pattern Recognition*, 2022. [3](#)
- [35] Olaf Ronneberger, Philipp Fischer, and Thomas Brox. U-net: Convolutional networks for biomedical image segmentation. In *Medical image computing and computer-assisted intervention–MICCAI 2015*, 2015. [3](#)
- [36] Chitwan Saharia, William Chan, Huiwen Chang, Chris Lee, Jonathan Ho, Tim Salimans, David Fleet, and Mohammad Norouzi. Palette: Image-to-image diffusion models. In *ACM SIGGRAPH 2022 conference proceedings*, 2022. [2](#)
- [37] Chitwan Saharia, William Chan, Saurabh Saxena, Lala Li, Jay Whang, Emily L Denton, Kamyar Ghasemipour, Raphael Gontijo Lopes, Burcu Karagol Ayan, Tim Salimans, et al. Photorealistic text-to-image diffusion models with deep language understanding. *Advances in Neural Information Processing Systems*, 2022. [3](#)
- [38] Tim Salimans and Jonathan Ho. Progressive distillation for fast sampling of diffusion models. *arXiv:2202.00512*, 2022. [3](#)
- [39] Uriel Singer, Adam Polyak, Thomas Hayes, Xi Yin, Jie An, Songyang Zhang, Qiyuan Hu, Harry Yang, Oron Ashual, Oran Gafni, et al. Make-a-video: Text-to-video generation without text-video data. *arXiv:2209.14792*, 2022. [2](#)
- [40] Jascha Sohl-Dickstein, Eric Weiss, Niru Maheswaranathan, and Surya Ganguli. Deep unsupervised learning using nonequilibrium thermodynamics. In *International Conference on Machine Learning*, 2015. [3](#)
- [41] Jiaming Song, Chenlin Meng, and Stefano Ermon. Denoising diffusion implicit models. *arXiv:2010.02502*, 2020. [3](#), [6](#)
- [42] Yang Song, Jascha Sohl-Dickstein, Diederik P Kingma, Abhishek Kumar, Stefano Ermon, and Ben Poole. Score-based generative modeling through stochastic differential equations. *arXiv:2011.13456*, 2020. [3](#)
- [43] Zhou Wang, Alan Conrad Bovik, Hamid R. Sheikh, and Eero P. Simoncelli. Image quality assessment: from error visibility to structural similarity. *IEEE Transactions on Image Processing*, 2004. [6](#), [1](#)
- [44] Jay Zhangjie Wu, Yixiao Ge, Xintao Wang, Stan Weixian Lei, Yuchao Gu, Yufei Shi, Wynne Hsu, Ying Shan, Xiaohu Qie, and Mike Zheng Shou. Tune-a-video: One-shot tuning of image diffusion models for text-to-video generation. In *Proceedings of the IEEE/CVF International Conference on Computer Vision*, 2023. [2](#), [3](#), [6](#), [7](#)
- [45] Zhen Xing, Qi Dai, Han Hu, Zuxuan Wu, and Yu-Gang Jiang. Simda: Simple diffusion adapter for efficient video generation. In *Proceedings of the IEEE/CVF Conference on Computer Vision and Pattern Recognition*, 2024. [6](#), [7](#)
- [46] Zhen Xing, Qi Dai, Han Hu, Zuxuan Wu, and Yu-Gang Jiang. Simda: Simple diffusion adapter for efficient video generation. In *Proceedings of the IEEE/CVF Conference on Computer Vision and Pattern Recognition*, 2024. [3](#)
- [47] Lvmin Zhang, Anyi Rao, and Maneesh Agrawala. Adding conditional control to text-to-image diffusion models. In *Proceedings of the IEEE/CVF International Conference on Computer Vision*, 2023. [3](#)
- [48] Yabo Zhang, Yuxiang Wei, Dongsheng Jiang, Xiaopeng Zhang, Wangmeng Zuo, and Qi Tian. Controlvideo: Training-free controllable text-to-video generation. *arXiv:2305.13077*, 2023. [3](#)
- [49] Guangcong Zheng, Xianpan Zhou, Xuewei Li, Zhongang Qi, Ying Shan, and Xi Li. Layoutdiffusion: Controllable diffusion model for layout-to-image generation. In *Proceedings of the IEEE/CVF Conference on Computer Vision and Pattern Recognition*, 2023. [2](#)
- [50] Yuanzhi Zhu, Zhaohai Li, Tianwei Wang, Mengchao He, and Cong Yao. Conditional text image generation with diffusion models. In *Proceedings of the IEEE/CVF Conference on Computer Vision and Pattern Recognition*, 2023. [2](#)

Teaching Video Diffusion Model with Latent Physical Phenomenon Knowledge

Supplementary Material

7. Criteria

Root Mean Square Error (RMSE). RMSE provides a comprehensive measure of pixel-level deviations between the generated and real videos. A lower RMSE indicates that the generated video is closer to the real video in terms of pixel values. The formula is as follows:

$$\text{RMSE} = \frac{1}{N} \sum_{t=1}^N \sqrt{\frac{1}{M} \sum_{i=1}^M (X_i^{\text{real}} - X_i^{\text{gen}})^2}, \quad (14)$$

where N is the number of frames, and M is the total number of pixels per frame. $\langle \cdot \rangle^{\text{real}}$ and $\langle \cdot \rangle^{\text{gen}}$ are true values and generated values respectively, as well as X_i are pixel values.

Structural Similarity Index Measure (SSIM). SSIM [43] assesses structural similarity between generated and real video frames, focusing on aspects like brightness, contrast, and texture. This metric helps ensure that the generated video maintains the structural integrity of the real video. Higher SSIM values indicate greater similarity. The formula is:

$$\text{SSIM} = \frac{(2\mu_x\mu_y + C_1)(2\sigma_{xy} + C_2)}{(\mu_x^2 + \mu_y^2 + C_1)(\sigma_x^2 + \sigma_y^2 + C_2)}, \quad (15)$$

where μ_x and μ_y are the mean values, σ_x and σ_y are the variances of frames x and y , σ_{xy} is the covariance, and C_1 and C_2 are constants to stabilize the division.

Additionally, to evaluate the generated video's quality, we analyze the velocity fields derived from optical flow based on physical quantities such as velocity, temperature, and volume fraction in the original video. This allows us to apply metrics that assess the alignment of the generated video with the original's physical characteristics. These metrics, grounded in convective dynamics, are suitable for analyzing the flow consistency across different physical quantities, determining if they exhibit smooth and realistic motion over time.

We compute the optical flow fields using the Farneback method [8], a dense optical flow estimation technique that approximates each pixel's local neighborhood as a polynomial function. This approach facilitates precise, pixel-wise motion estimates, making it ideal for capturing fine-grained movements in fluid-related fields.

In Farneback's method, each pixel neighborhood is represented by a quadratic polynomial:

$$f(\mathbf{x}) = \mathbf{x}^\top \mathbf{A} \mathbf{x} + \mathbf{b}^\top \mathbf{x} + c, \quad (16)$$

where \mathbf{x} is the pixel location, \mathbf{A} represents second-order terms, \mathbf{b} denotes first-order terms, and c is a constant. The displacement vector \mathbf{d} , representing pixel-wise motion, is derived from changes in these terms across frames:

$$\mathbf{d} = -(\mathbf{A} + \mathbf{A}^\top)^{-1}(\mathbf{b} - \mathbf{b}'). \quad (17)$$

Using a pyramidal approach, the Farneback algorithm captures motion at multiple scales, refining the motion field at each level for accurate displacement estimation. The resulting optical flow vectors $\mathbf{u} = (u, v)$ provide the basis for calculating metrics that evaluate the generated video's fidelity to the physical properties of the original.

Stream Function Error (SFE). The stream function, ψ , represents a scalar field from which the velocity components of a two-dimensional incompressible flow can be derived, where $\partial\psi/\partial y = u$ and $\partial\psi/\partial x = -v$ [26]. For optical flow fields, ψ is computed via numerical integration:

$$\psi(x, y) = \int u \, dy - \int v \, dx. \quad (18)$$

The Stream Function Error (SFE) between generated and real data is calculated as:

$$\text{SFE} = \frac{1}{N} \sum_{t=1}^N \sqrt{\frac{1}{M} \sum_{i=1}^M (\psi_i^{\text{real}} - \psi_i^{\text{gen}})^2}. \quad (19)$$

SFE assesses the dynamic consistency of the generated flow field with the real flow by comparing streamline characteristics. Lower SFE values indicate that the generated flow better replicates advective properties, providing insights into the physical accuracy and quality of the generated video.

Smoothness Error (SE). Smooth changes in velocity generally reflect the asymptotic behavior of physical phenomena, while abrupt fluctuations may be unrealistic [18]. Temporal smoothness in optical flow velocity can capture the steady propagation characteristics of the underlying physical quantities. Smoothness Error (SE) measures the timewise smoothness of both the generated and real flow fields, providing insight into physical continuity over time. SE is defined as:

$$\text{SE} = \frac{1}{N-1} \sum_{t=1}^{N-1} \sqrt{\frac{1}{M} \sum_{i=1}^M (\Delta u_i^{\text{gen}} - \Delta u_i^{\text{real}})^2}, \quad (20)$$

where $\Delta u_i = u_{i,t+1} - u_{i,t}$ represents the velocity change across consecutive time intervals. A lower SE value

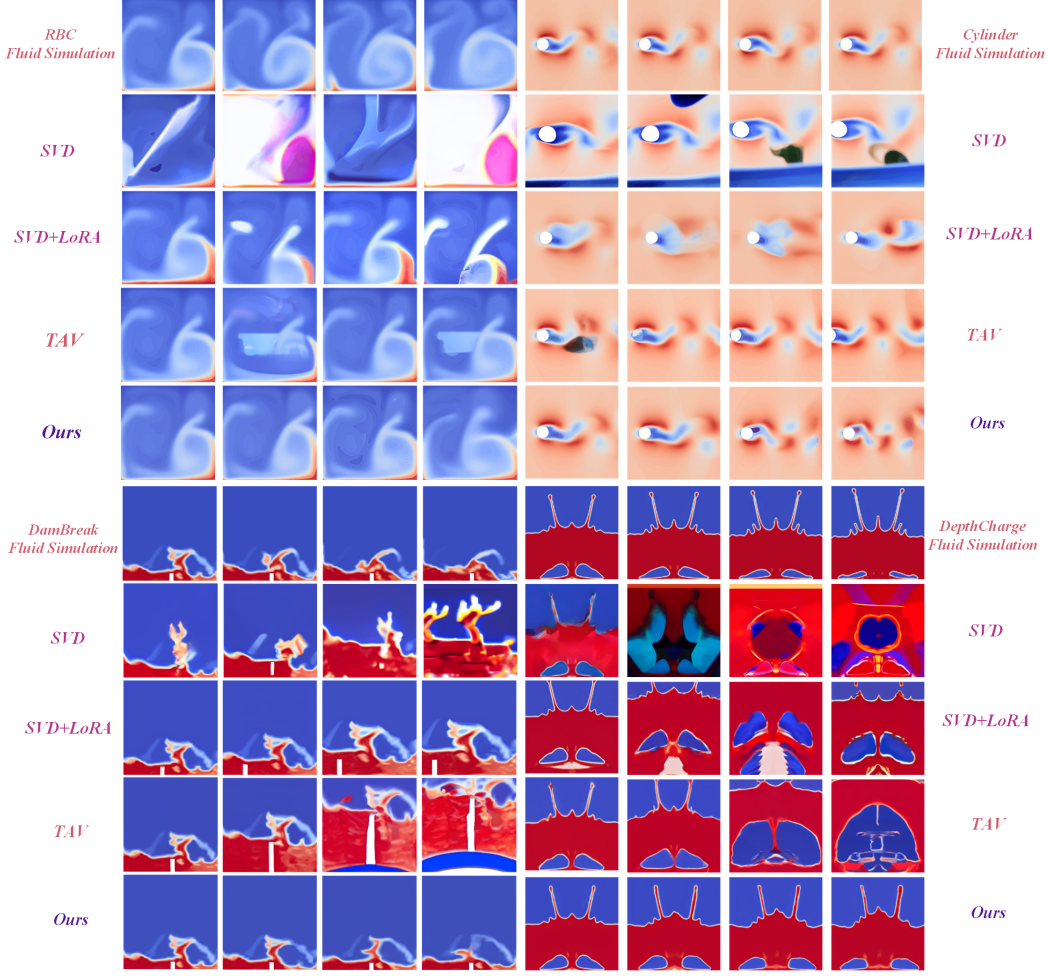


Figure 6. Qualitative comparisons in fluid simulation dataset. Though incorporating physical phenomenon knowledge, our method generates rational phenomena that exhibit better alignment with physical laws.

indicates greater temporal smoothness in the generated flow, reflecting the essential physical continuity of the quantity.

Gradient Smoothness (GS). Gradient Smoothness evaluates the temporal smoothness of the gradient field in the generated frames, capturing the physical continuity of spatial features across time steps. The formula is:

$$GS = \frac{1}{N-1} \sum_{t=1}^{N-1} \sqrt{\frac{\sum_{i=1}^M \left(\left(\frac{\partial X_i^{t+1}}{\partial x} - \frac{\partial X_i^t}{\partial x} \right)^2 + \left(\frac{\partial X_i^{t+1}}{\partial y} - \frac{\partial X_i^t}{\partial y} \right)^2 \right)}{2M}}. \quad (21)$$

This metric is computed solely from the generated frames

and reflects the smoothness of changes in the gradient field over time.

Continuity Score (CS). Continuity Score measures the spatial continuity of the generated optimal flow field by calculating the divergence of each frame in the generated sequence. The formula is:

$$CS = \frac{1}{N} \sum_{t=1}^N \sqrt{\frac{1}{M} \sum_{i=1}^M (\nabla \cdot \mathbf{u}_i)^2}, \quad (22)$$

where $\nabla \cdot \mathbf{u} = \partial u / \partial x + \partial v / \partial y$ represents the divergence of the generated velocity field $\mathbf{u} = (u, v)$ at each pixel i and time step t . Lower CS values indicate better preservation of spatial continuity in the generated field, reflecting adherence to mass conservation principles.

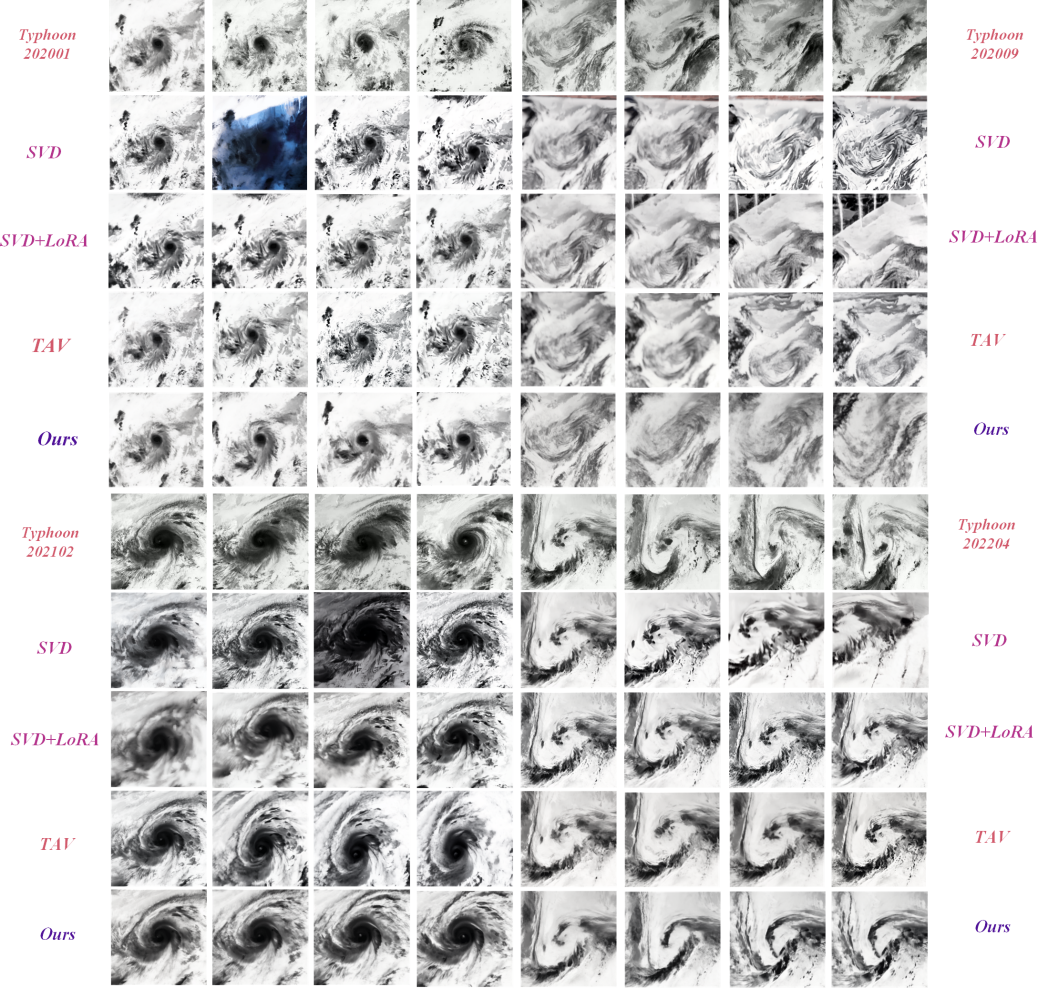


Figure 7. Qualitative comparisons in true typhoon dataset. Though incorporating physical phenomenon knowledge, our method generates rational phenomena that exhibit better alignment with physical laws.

Q-Criterion Error (QCE). The Q-Criterion identifies vortices within a flow field by balancing rotational and strain rates [16]. It's calculated as:

$$Q = \frac{1}{2} (\|\boldsymbol{\Omega}\|^2 - \|\mathbf{S}\|^2), \quad (23)$$

where $\boldsymbol{\Omega} = 1/2 (\nabla \mathbf{u} - (\nabla \mathbf{u})^T)$ is rotation tensor and $\mathbf{S} = 1/2 (\nabla \mathbf{u} + (\nabla \mathbf{u})^T)$ is strain tensor. In the two-dimensional plane, the calculation can be simplified as:

$$Q = \frac{1}{2} \left(-\left(\frac{\partial u}{\partial x}\right)^2 - \left(\frac{\partial v}{\partial y}\right)^2 - 2 \frac{\partial u}{\partial y} \frac{\partial v}{\partial x} \right), \quad (24)$$

with error:

$$\text{QCE} = \frac{1}{N} \sum_{t=1}^N \sqrt{\frac{1}{M} \sum_{i=1}^M (Q_i^{\text{gen}} - Q_i^{\text{real}})^2}. \quad (25)$$

Lower QCE suggests that the generated flow retains rotational structures similar to the real flow.

Vorticity Error (VE). Vorticity represents rotational effects, such as eddies and vortices, which are vital for processes like mixing, energy transfer, and turbulence development [17]. In two-dimensional flow, local rotation is quantified by vorticity, defined as:

$$\omega = \frac{\partial v}{\partial x} - \frac{\partial u}{\partial y}. \quad (26)$$

The Vorticity Error (VE) measures the accuracy of the generated flow's rotational dynamics compared to the real flow and is calculated as:

$$\text{VE} = \frac{1}{N} \sum_{t=1}^N \sqrt{\frac{1}{M} \sum_{i=1}^M (\omega_i^{\text{gen}} - \omega_i^{\text{real}})^2}. \quad (27)$$

Lower VE values indicate closer alignment in rotational characteristics, showing that the generated flow accurately replicates the real flow's dynamics.

8. CFD simulations

Rayleigh-Bénard convection is a thermally-driven natural convection flow caused by temperature differences, which induces ascending and descending currents and is commonly used to study turbulence and heat transfer. Cylinder flow simulates the fluid behavior around an obstacle (e.g., a cylinder), producing wake and vortex structures to examine vortex dynamics in bluff-body flows. DamBreak flow models the propagation of free-surface waves and fluid flow following a sudden dam collapse, illustrating gravity-driven, nonlinear free-surface behavior. DepthCharge flow simulates the high-pressure shockwave and bubble expansion dynamics following an underwater explosion, focusing on the transient changes at the water-air interface.

The numerical simulations for these flows were conducted using the open-source software OpenFOAM, which employs the finite volume method for discretizing partial differential equations (PDEs). The Rayleigh-Bénard convection was modeled with a RANS turbulence approach, while the other flows were treated as laminar. A second-order central difference scheme was applied to the diffusion terms, and appropriate discretization schemes were selected for the convection terms according to the specific physical requirements of each flow. Temporal discretization used a second-order backward implicit method for Rayleigh-Bénard convection, while a first-order explicit Euler scheme was applied for the others. The simulations were conducted over 400 time steps, with results interpolated from nonuniform grids to a uniform spatial resolution of 512×512 . The processed frames were then compiled into 16 videos.

9. Qualitative Comparisons.

To provide a more comprehensive analysis of the performance of our proposed method, we present additional qualitative comparisons. The visualization results are shown in Figure 6 and Figure 7, with Figure 6 illustrating the comparisons on the fluid simulation dataset and Figure 7 showing the results on the true typhoon dataset. These examples consistently highlight the superior performance of our method, showcasing its robustness and improved alignment with physical realism across various scenarios.

10. Provided Videos.

To directly assess the performance of our proposed method, we also provide a comprehensive review video, titled “Comparison Results.mp4”, which summarizes the results. Additional detailed videos corresponding to specific experiments can be found in the “sup videos” folder.